Geophys. J. Int. (2008) doi: 10.1111/j.1365-246X.2007.03696.x

Surface wave array tomography in SE Tibet from ambient seismic noise and two-station analysis – II. Crustal and upper-mantle structure

Huajian Yao,[1] Caroline Beghein[2] and Robert D. van der Hilst[1]

[1]*Department of Earth, Atmospheric, and Planetary Sciences, Massachusetts Institute of Technology, Cambridge,* MA 02139, *USA. E-mail: hjyao@mit.edu*
[2]*School of Earth and Space Exploration, Arizona State University, Tempe,* AZ 85287, *USA*

Accepted 2007 November 24. Received 2007 November 19; in original form 2007 June 23

SUMMARY

We determine the 3-D shear wave speed variations in the crust and upper mantle in the southeastern borderland of the Tibetan Plateau, SW China, with data from 25 temporary broad-band stations and one permanent station. Interstation Rayleigh wave (phase velocity) dispersion curves were obtained at periods from 10 to 50 s from empirical Green's function (EGF) derived from (ambient noise) interferometry and from 20 to 150 s from traditional two-station (TS) analysis. Here, we use these measurements to construct phase velocity maps (from 10 to 150 s, using the average interstation dispersion from the EGF and TS methods between 20 and 50 s) and estimate from them (with the Neighbourhood Algorithm) the 3-D wave speed variations and their uncertainty. The crust structure, parametrized in three layers, can be well resolved with a horizontal resolution about of 100 km or less. Because of the possible effect of mechanically weak layers on regional deformation, of particular interest is the existence and geometry of low (shear) velocity layers (LVLs). In some regions prominent LVLs occur in the middle crust, in others they may appear in the lower crust. In some cases the lateral transition of shear wave speed coincides with major fault zones. The spatial variation in strength and depth of crustal LVLs suggests that the 3-D geometry of weak layers is complex and that unhindered crustal flow over large regions may not occur. Consideration of such complexity may be the key to a better understanding of relative block motion and patterns of seismicity.

Keywords: Interferometry; Surface waves and free oscillations; Seismic tomography; Crustal structure; Asia.

1 INTRODUCTION

The Tibetan Plateau is the result of the collision of the Indian and Eurasian Plates during the Cenozoic, which began some 50 Ma (Molnar & Tapponnier 1975; Rowley 1996). Different from the central collision zone, the southeast borderland of the Tibetan Plateau (from western Sichuan to central Yunnan in southwest China, Fig. 1a) is characterized by a gentle slope, lack of large-scale young crustal shortening and a predominance of N–S-trending strike-slip faults (Royden *et al.* 1997). These deformation characteristics have been attributed to ductile channel flow in a weak lower crust (Royden *et al.* 1997; Clark & Royden 2000; Shen *et al.* 2001), but many first-order questions remain about the presumed weak zones. Using high-resolution surface wave (array) tomography, in this paper, we seek to establish the existence of weak crustal flow channels, map out their lateral extent and determine which part of the crust is actually involved. Research targets of particular interest are crustal zones of low shear wave speed and/or low electric resistivity, since they are often considered as diagnostic for low strength, or the presence of partial melt.

The study region represents the eastern part of the Lhasa block and comprises three major active fault systems (Fig. 1b): the left-lateral Xianshuihe-Xiaojiang fault system, the right-lateral Red River fault system and the left-lateral Dali fault systems, among which the Xianshuihe-Xiaojiang fault system is the most active (Wang *et al.* 1998; Wang & Burchfiel 2000). The diamond-shaped crustal fragment bounded by these fault systems is usually interpreted as a tectonic terrane, called the Chuan-Dian Fragment (Fig. 1b; Kan 1977; Wang *et al.* 1998). The crustal motion of this fragment is dominated by a clockwise rotation around the eastern Himalayan Syntaxis (EHS), as revealed by geodetic measurements (King *et al.* 1997; Chen *et al.* 2000; Zhang *et al.* 2004; Shen *et al.* 2005) and geological studies (Wang *et al.* 1998; Wang & Burchfiel 2000), which suggests an eastward or southeastward extrusion of crustal material from the central and eastern part of the plateau.

Regional traveltime tomography studies (Huang *et al.* 2002; Wang *et al.* 2003; Li *et al.* 2006, 2008) have revealed large velocity variations in the lithosphere of southwest China, including prominent low velocity anomalies in the crust and upper mantle in western Sichuan and in the Tengchong volcanic area. Receiver function analyses (Hu

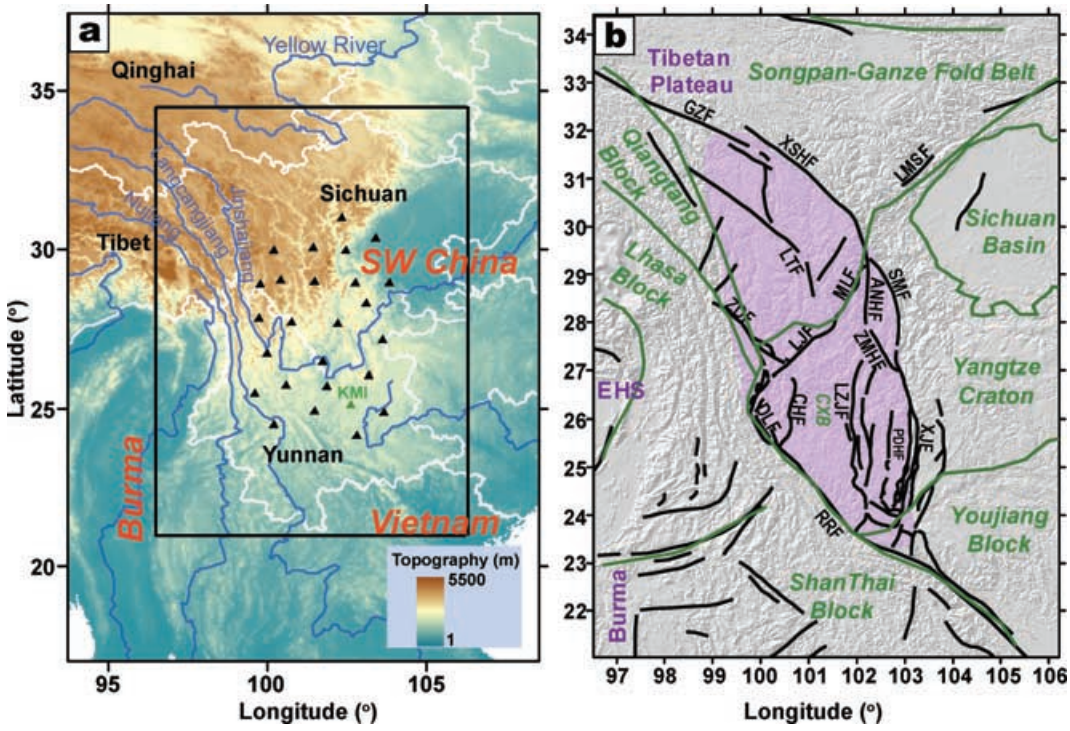

Figure 1. (a) Geographic map of SW China and adjacent areas. White lines show provincial boundaries in China; blue lines depict major rivers. The MIT-CIGMR array stations are depicted as black triangles and the permanent station KMI is shown as the green triangle. The black box outlines the study region shown in (b). (b) Tectonic elements and fault systems in the southeastern borderland of the Tibetan Plateau. Tectonic boundaries (modified from Li 1998 and Tapponnier *et al.* 2001) are shown as dark green lines. The magenta shaded area shows the approximate region of the Chuan-Dian Fragment. The major faults are depicted with black lines (after Wang *et al.* 1998; Wang & Burchfiel 2000; Shen *et al.* 2005). Abbreviations are: GZF, Ganzi Fault; LMSF, Longmenshan Fault; XSHF, Xianshuihe Fault; LTF, Litang Fault; ANHF, Anninghe Fault; SMF, Shimian Fault; ZMHF, Zemuhe Fault; ZDF, Zhongdian Fault; LJF, Lijiang Fault; MLF, Muli Fault; DLF, Dali Fault; CHF, Chenghai Fault; LZJF, Luzhijiang Fault; PDHF, Pudude Fault; XJF, Xiaojiang Fault; RRF, Red River Fault; CXB, Chuxiong Basin and EHS, Eastern Himalaya Syntaxis.

et al. 2005a; Xu *et al.* 2007) have shown that in SW China low velocity layers (LVLs) exist not only between 10 and 15 km depth (in sedimentary basins), but also between 30 and 40 km depth (that is, the middle to lower crust) and that the Poisson's ratio in this region is generally high. Joint inversion of surface wave and receiver function data (Hu *et al.* 2005b) revealed low-velocity layers in the upper mantle beneath areas in central Yunnan and Yunnan–Myanmar–Thailand that are also characterized by high heat flow (Hu *et al.* 2000) and major earthquakes (Huang *et al.* 2002). In this region, wide-angle seismic profiles in western Yunnan show that seismic reflections from the middle-lower crust are weak (Zhang *et al.* 2005). Furthermore, shear wave splitting studies have revealed a complex pattern of anisotropy, with a dramatic change in fast polarization direction across the Chuan-Dian Fragment. Mantle anisotropy occurs at large angles with structural trends at the surface, which is consistent with (but does by itself not require) weak crust–mantle coupling (Lev *et al.* 2006; Sol *et al.* 2007).

Magnetotelluric (MT) sounding has revealed a large-scale low resistivity layer at more than 10 km depth beneath northern part of the Chuan-Dian Fragment (Sun *et al.* 2003). Bai *et al.* (2006) provided evidence for low resistivity in the middle/lower crust between the Jinsha River suture zone and the Xianshuihe fault along latitude $\sim 30^{\circ}$, and also between the Red River fault and the Xiaojiang fault along latitude $\sim 25^{\circ}$.

Collectively, the seismological and magnetotelluric evidence is consistent with the view that the southeastern margin of the Tibetan Plateau is underlain by a weak middle-lower crust. However, due to the specific resolution limitations of each of these methods, the vertical and horizontal extent of the low velocity (or resistivity) zones has remained enigmatic, and the level of interconnectedness between the different low velocity zones is not known. Body wave traveltime tomography usually does not have good depth resolution, especially in the crust part. For MT studies, the upper boundary of the low resistivity layer can be well resolved but the lower boundary is usually unconstrained. Receiver functions resolve interfaces with large velocity contrast quite well, but are less sensitive to absolute wave speed values. Moreover, interpolation between stations may not be justified across major fault systems.

The dispersion of short-period surface waves is more sensitive to shallow heterogeneity than phase arrival times of steeply incident body waves, and it provides more accurate constraints on shear wave speeds than receiver functions. Traditional dispersion analysis, however, does not yield reliable estimates of the structure in the shallow crust because of strong scattering at short periods ($T <$ 30 s). Recent advances in surface wave ambient noise tomography (e.g. Sabra *et al.* 2005; Shapiro *et al.* 2005; Yao *et al.* 2006; Lin *et al.* 2007; Yang *et al.* 2007) greatly enhance our ability to resolve the shallow crustal structure. This approach involves measuring the dispersion of empirical Green's functions (EGFs) obtained from cross-correlation of time-series containing ambient noise.

Yao *et al.* (2006), hereinafter referred to as Paper I, introduced a method for multiscale surface wave array tomography that combines Rayleigh wave phase velocity measurements from the traditional two-station (TS) analysis and the EGF estimated from

(ambient noise) interferometry. In this paper, we improve the dispersion measurements (both for the EGF and the TS analysis), construct phase velocity maps in the period band 10–150 s, and invert them for 3-D shear wave speed variations in the crust and upper mantle beneath the southeastern borderland of the Tibetan Plateau using the Neighbourhood Algorithm (NA) (Sambridge 1999a,b). NA is an inversion approach, based on forward modelling, that searches the entire model space and identifies all models that fit the observations (here, the dispersion data) and produces quantitative measures of parameter trade-offs and uncertainties. NA differs from direct search techniques, such as LSQR (Nolet 1985), which select a single model (subject to a particular, often subjective regularization) that optimizes a cost function. NA has previously been used for *P* and *S* tomography using normal-mode and surface wave data (Beghein *et al.* 2002), non-linear waveform inversion (Yoshizawa & Kennett 2002) and *S*-wave velocity structure inversion from surface wave data (Snoke & Sambridge 2002).

We present the tomography model (i.e. 3-D shear wave speeds and their uncertainty) of the crust and upper mantle beneath the southeastern borderland of the Tibetan Plateau, SW China, with special emphasis on intracrustal low velocity zones and their implications for our understanding of the present-day seismo-tectonic setting of the region and the dynamic evolution of the Tibetan Plateau.

2 DATA

From 2003 September to 2004 October MIT and the Chengdu Institute of Geology and Mineral Resources (CIGMR) operated an array of 25 three-component, broad-band seismometers in the Sichuan and Yunnan provinces, SW China (Fig. 1a) to investigate the structure and geological evolution of the eastern Tibetan Plateau. Seismograms from this array have been used for traveltime tomography (Li *et al.* 2008), receiver function analysis (Xu *et al.* 2007) and shear wave splitting (Lev *et al.* 2006; Sol *et al.* 2007).

2.1 Phase velocities from EGF analysis

In Paper I, we present a method for measuring Rayleigh wave phase velocity dispersion from EGF analysis. In that paper, we obtained EGFs from 4 months of data (April 2004–July 2007) and then measured phase velocities between the MIT–CIGMR array stations. Here we redo the analysis and construct vertical component EGFs from 10 months long (continuous) records, and in addition to the MIT–CIGMR array we used data from KMI, a permanent (Global Seismograph Network) station in Kunming, Yunnan (Fig. 1a). The use of the longer records increased the signal-to-noise ratio (in the EGFs) and resulted in better path coverage. Due to the uneven distribution of noise sources, the positive time and negative time parts of EGFs are, in general, not time-symmetrical (Yao *et al.* in preparation). For each interstation path, we average the causal and acausal parts of the EGF to produce the symmetrical component (Yang *et al.* 2007) and enhance the signal-to-noise ratio. From the symmetrical component of EGFs we then measure Rayleigh wave phase velocity dispersion within the period band 10–50 s. The green line in Fig. 2(a) shows the number of measurements (or paths) at each period, which decreases as the period increases due to the far-field approximation for surface waves representation (Paper I). The average dispersion curve in the period band 10–50 s from EGF analysis is shown as the green line in Fig. 2(b).

2.2 Phase velocities from TS analysis

To obtain phase velocity dispersion at larger periods we follow the procedures outlined in Paper I and measure the dispersion from 20 to 150 s using the TS analysis. For the MIT–CIGMR array and KMI we obtained about 1700 interstation dispersion curves from about 200 earthquakes at teleseismic distances (and for deviation angles α and β—defined in Paper I—less than 3° and 7°, respectively). For each station pair we average the dispersion curves from different events to obtain the input for the phase velocity and standard error calculations. The total number of paths at each period is shown in Fig. 2(a) (black line). The regional average dispersion curve from TS analysis is shown Fig. 2(b). The relative standard error (Fig. 2b) is about 1–1.5 per cent for the periods considered here.

2.3 Phase velocities from EGF + TS averaging

For periods between 20 and 50 s the average phase velocities from the TS and EGF analysis are similar. Indeed, the discrepancy is generally less than 1 per cent, which is smaller than the standard errors of either method and much smaller than the difference with the reference values according to *ak135*. Compared to Paper I, we note a substantial

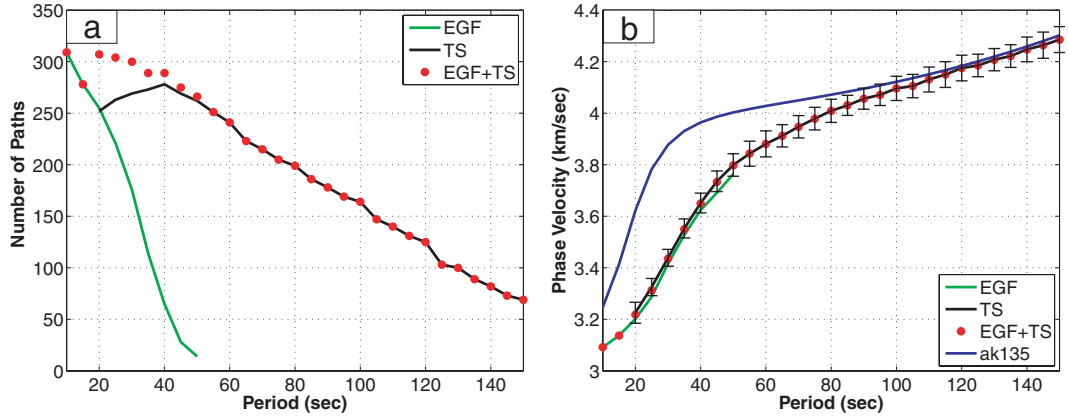

Figure 2. (a) Number of interstation paths at different periods from the EGF analysis (green line), TS analysis (black line) and EGF + TS averaging (red dots); (b) the average dispersion curve for the array area from the EGF analysis (green line), TS analysis (black line) and EGF+TS averaging (red dots). The black error bars in (b) are the average standard errors for the average dispersion curve from the TS analysis. The blue line in (b) is the Rayleigh wave phase velocity dispersion curve (fundamental mode) predicted from the global *ak135* (continental) model (Kennett *et al.* 1995).

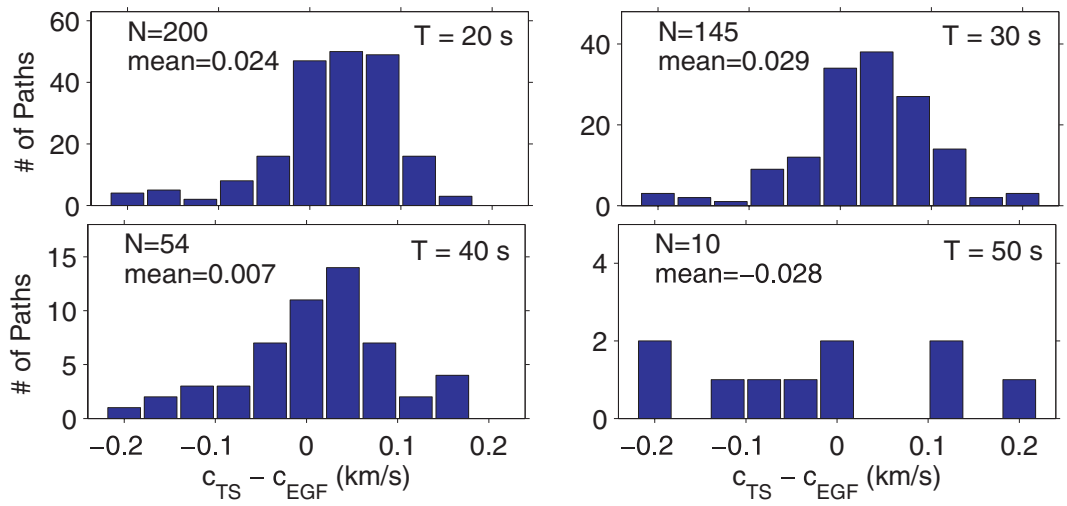

Figure 3. Histogram to show the comparison of interstation Rayleigh wave phase velocity measurements from the TS and EGF analysis at overlapping periods (20–50 s). The horizontal axis show the difference between the phase velocity from the TS analysis (C_{TS}) and that from the EGF analysis (C_{EGF}), that is, $C_{TS} - C_{EGF}$, while the vertical axis shows the number of interstation paths which falls in the different $C_{TS} - C_{EGF}$ interval each with a width of 0.04 km s^{-1}. In each plot, 'N' is the total number of paths for comparison and 'mean' is the average difference (km s^{-1}) of $C_{TS} - C_{EGF}$ for all paths at that period.

increase in quality of the phase velocity measurements, which we attribute to the use of longer cross-correlation time windows for the EGF measurement and the larger number of TS measurements. In Fig. 3 we compare (for the period band they have in common) the TS and EGF measurements for the same tow-station pairs. The average phase velocities from TS analysis can be up to 1 per cent higher than those from the EGF analysis. This difference can be due to differences in sensitivity to structure (Paper I) and to imperfect recovery of the surface wave Green's functions due to the unknown but certainly inhomogeneous distribution of noise sources (Yao *et al.* in preparation). However, within reasonable uncertainty, the EGF and TS methods appear to yield similar results.

The input interstation dispersion data for the calculation of phase velocity maps between 10 and 150 s is obtained as follows. For periods smaller than 20 s we use the results of interferometry (i.e. the EGFs) and for periods between 50 and 150 s we use the TS results. For periods between 20 and 50 s we take the mean of the phase velocity from the EGF analysis (C_{EGF}) and the TS analysis (C_{TS}) if $|C_{EGF} - C_{TS}| \leq 0.1$ km s^{-1}, C_{TS} if $|C_{EGF} - C_{TS}| > 0.1$ km s^{-1} (and if either at least five measurements from TS analysis have been made for that period or the standard error of phase velocity measurement at that period is less than 0.04 km s^{-1}), or C_{EGF} in all other cases. The number of (average) phase velocity measurements (or paths) at each period is shown as the red dot in Fig. 2(a). As expected, the number of paths for the overlapping periods after averaging the TS and EGF measurements is larger than that from either method alone. This averaging scheme mitigates the problem that the number of EGFs measurements decreases sharply as the period increases (Fig. 2a) and greatly enhances the path coverage and the reliability of measurements for the TS analysis at shorter periods.

3 PHASE VELOCITY MAPS

Following Paper I, we construct 2-D phase velocity maps from 10 to 150 s. The path distributions for six different periods (10, 30, 60, 90, 120 and 150 s) are shown in Fig. 4. At each period the data coverage is denser than in Paper I, especially at the longer periods. The corresponding phase velocity maps are shown in Fig. 5. The lateral resolution in these maps is generally of the order of (or less than) the interstation distance (∼100 km). From the maps, we infer the phase velocity as a function of frequency at each point of the 0.5° × 0.5° grid that is used to parametrize the study region.

4 STRUCTURE INVERSION USING NEIGHBOURHOOD ALGORITHM (NA)

4.1 NA optimization

The NA involves two stages (Sambridge 1999a,b). The first stage consists of a model space search to identify the 'good' data fitting regions. It employs a geometrical construct—the Voronoi cells—to drive the search towards the best data-fitting regions while continuing to sample a relatively wide variety of different models. The use of these cells makes this algorithm self-adaptative because, with a good choice of some tuning parameters, one can explore the complete model space with the possibility to jump out of a local minimum. It also has the advantage of being able to sample several promising regions simultaneously. During this search, the sampling density increases in the surroundings of the good models without losing information on the models previously generated (even the 'bad' ones). The first stage results in a distribution of misfits, which serves to approximate the posterior probability density function (PPDF).

In the second stage of NA, a sampling of this distribution generates a 'resampled ensemble' that follows the PPDF. This resampled ensemble is then integrated numerically to compute the likelihood associated with each model parameter, also called 1-D marginal PPDFs (or 1-D marginals), the correlation matrix and 2-D marginal PPDFs (or 2-D marginals). The departure of these 1-D marginals from a Gaussian distribution can be used as a diagnostic of the degree of ill-posedness of the problem. In addition, their width can be seen as a more realistic measure of model uncertainty than one we obtain from traditional inversion techniques. The 2-D marginals quantify the trade-offs between two variables. (NB the same information can be deduced from the correlation matrix if a Gaussian

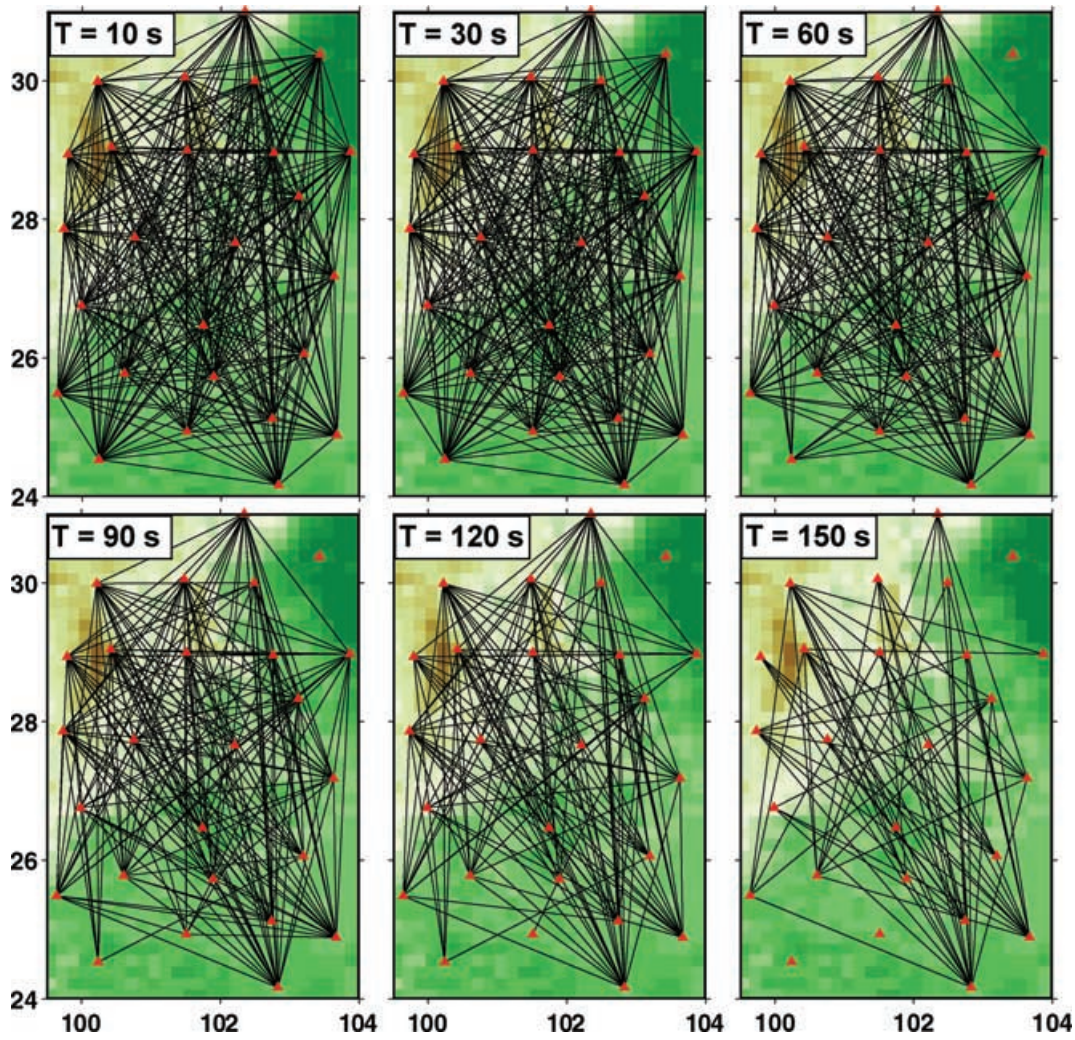

Figure 4. Interstation ray path distribution for phase velocity measurements after EGF + TS averaging for six different periods (10, 30, 60, 90, 120 and 150 s). The stations are shown as red triangles.

approximation of the model space could be made.) Since they characterize the entire ensemble of models compatible with the data, the 1-D and 2-D marginals are powerful instruments for estimating true resolution and uncertainty of model parameters.

4.2 Model space parametrization and misfit function

From the phase velocity as function of period we estimate with NA the shear wave speed as a function of depth at all gridpoints in the study area. At each location, we parametrize the inversion problem using nine parameters: these are Moho depth and the shear wave speeds in eight (non-overlapping) depth intervals in the crust and upper mantle. The detail of the parameters as well as their perturbation range with respect to the reference model is shown in Table 1. The mantle part of the reference model follows the global *ak135* model (Kennett *et al.* 1995). The crust part of the model is parametrized by means of three layers (upper, middle and lower crust); for each gridpoint, the Moho depth inferred from receiver functions (Xu *et al.* 2007) represents the reference value for total crustal thickness, and the upper, middle and lower crust are set to about 1/3 of the total crustal thickness. We allow the Moho depth to vary within 5 km above or below the reference Moho depth, and the thickness of the lower crustal and uppermost mantle layer will change accordingly.

Because of the evanescent character of the surface waves, the sensitivity of the data to changes in wave speed decreases with increasing depths, and for depth larger than 280 km we simply adopt *Vp*, *Vs* and ρ from the *ak135* model. Because short period (e.g. $T < 40$ s) Rayleigh waves are also sensitive to *Vp* and ρ in the shallow crust (Mooney *et al.* 1998; Simons & van der Hilst 2003), we also account for the sensitivity of Rayleigh wave phase velocity to perturbations in *Vp* and ρ. In the first stage of the NA, for each layer in the crust, once *Vs* is given, *Vp* and ρ in that corresponding layer are calculated from *Vs* using the empirical relations between elastic wave speeds and density in the Earth's crust (Brocher 2005). In each of the five upper-mantle layers, the perturbation in shear wave speed is ± 0.6 km s^{-1} with respect to the reference value from the value of *ak135* at pertinent depths. The reference values of *Vp* and ρ in each upper-mantle layer are also taken directly from the *ak135*. [We remark that we do not apply the empirical relationships by Brocher (2005) for the lithospheric mantle because they are only valid for crustal rocks.] For each upper-mantle layer, when a perturbation ΔVs is produced with respect to the reference *Vs*, the perturbations

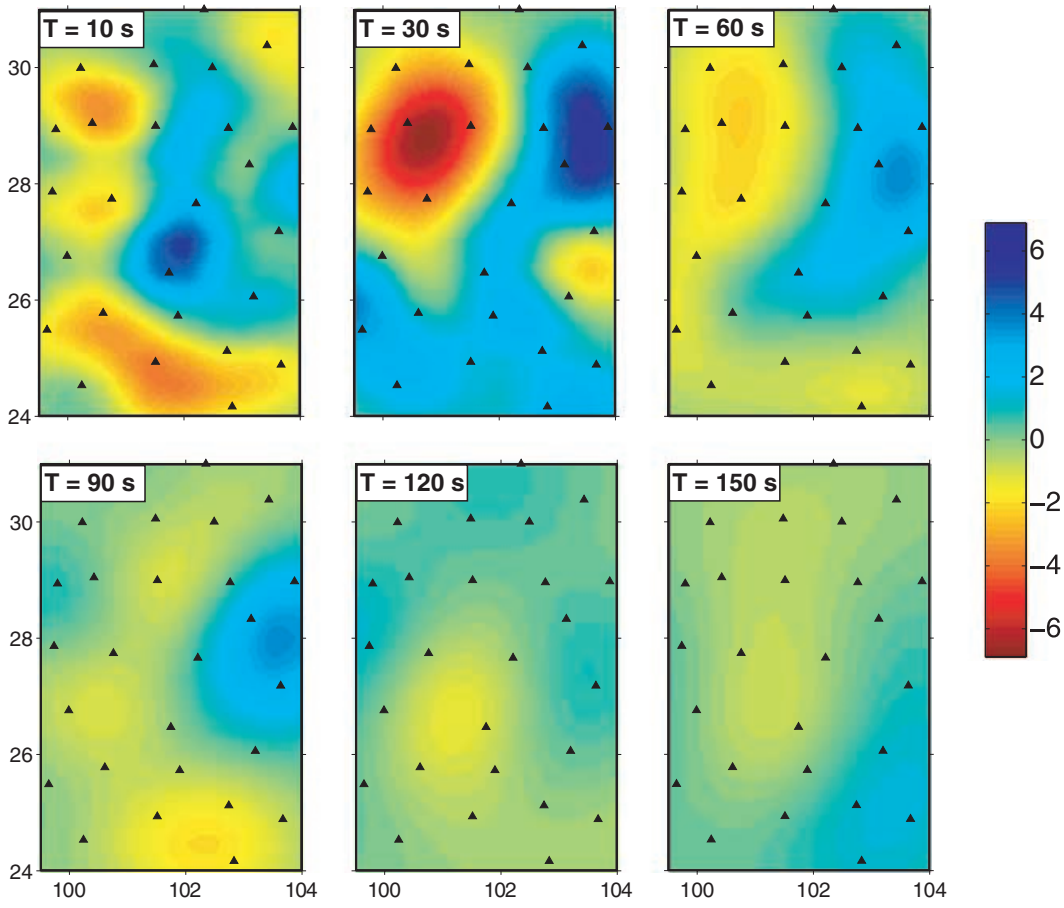

Figure 5. Perturbation (in percentage) of 2-D phase velocity maps at 6 different periods (10, 30, 60, 90, 120 and 150 s) with respect to the average phase velocities (red dots in Fig. 2(b)) constructed from the dispersion data after EGF + TS averaging. The corresponding ray path distribution map at each period is shown in Fig. 4. The stations are shown as black triangles.

Table 1. Model parameters as well as their reference value, perturbation range, and average perturbation in NA.

Name of model parameter	Reference value of parameter	Perturbation with respect to the reference value	Average perturbation
Moho depth	H (km)	[−5 5] km	−0.32 km
Vs in the upper crust	3.4 km s^{-1}	[−0.8 0.4] km s^{-1}	−0.069 km s^{-1}
Vs in the middle crust	3.6 km s^{-1}	[−0.8 0.4] km s^{-1}	−0.192 km s^{-1}
Vs in the lower crust	3.8 km s^{-1}	[−0.8 0.4] km s^{-1}	−0.120 km s^{-1}
Vs in Moho – 90 km	*Vs* from *ak135* (km s^{-1})	[−0.6 0.6] km s^{-1}	−0.197 km s^{-1}
Vs in 90–130 km	*Vs* from *ak135* (km s^{-1})	[−0.6 0.6] km s^{-1}	−0.053 km s^{-1}
Vs in 130–170 km	*Vs* from *ak135* (km s^{-1})	[−0.6 0.6] km s^{-1}	0.102 km s^{-1}
Vs in 170–220 km	*Vs* from *ak135* (km s^{-1})	[−0.6 0.6] km s^{-1}	0.130 km s^{-1}
Vs in 220–280 km	*Vs* from *ak135* (km s^{-1})	[−0.6 0.6] km s^{-1}	0.058 km s^{-1}

H denotes the reference Moho depth from teleseismic receiver functions (Xu *et al.* 2007) and *Vs* is shear wave speed (km s^{-1}). 'Average Perturbation' in the fourth column means the average perturbation of the model parameters for all gridpoints in the study region. The average Moho depth is 49.87 km from receiver functions (Xu *et al.* 2007) and 49.55 km after NA.

of *P*-wave speed (ΔVp) and density ($\Delta\rho$) with respect to the *ak135* values for that layer are also obtained using the following relations (Masters *et al.* 2000):

$$\frac{\mathrm{d}\ln V_p}{\mathrm{d}\ln V_s} = 0.6, \quad \frac{\mathrm{d}\ln \rho}{\mathrm{d}\ln V_s} = 0.4. \tag{1}$$

Through the use of relationships among *Vs*, *Vp* and ρ for the crustal and mantle layers, we thus incorporate the influence of *Vp* and ρ on the phase velocities in NA.

For every model generated in the NA model space search, Rayleigh wave phase velocities are calculated in the period band 10–150 s. To calculate misfit we use the L_2-norm to represent the distance between the predicted and the observed dispersion data

$$\Phi = \left\{ \frac{1}{N} \sum_{i=1}^{N} \left(\frac{c_i^{\mathrm{pred}} - c_i^{\mathrm{obs}}}{\sigma_i} \right)^2 \right\}^{1/2}, \tag{2}$$

where N is the total number of periods at which the phase velocity is measured; c_i^{pred} and c_i^{obs} is the predicted and observed phase velocity at the i^{th} period, respectively; σ_i is the estimated standard error of the observed phase velocity at the i^{th} period. In this study, $N = 25$,

and σ_i is set to be $0.01c_i^{\rm obs}$ because the standard error of interstation phase velocity measurements is about 1 per cent (Yao *et al.* 2006).

Each stage of the NA requires the tuning of parameters whose optimum values have to be found by trial and error. Several authors have described the influence of these parameters on the survey of the model space and on the Bayesian interpretation of the results (e.g. Sambridge 1999a,b; Resovsky & Trampert 2002). To broaden the survey in the model space and to consider the speed of convergence of the algorithm, the total number of new models generated at each iteration step, n_s, is set to 100, and the number of best data-fitting cells in which the new models are created, n_r, is set to 50 after a set of stability and convergence tests.

4.3 Example of NA optimization

We use the dispersion data, the solid dots with error bars in Fig. 6(a), at the gridpoint at (101°E, 29°N) to illustrate the performance of NA. Note that the observed phase velocities in the short and intermediate period range (10–80 s) are much lower than those predicted from the reference model (dashed line in Fig. 6a), which indicates a possible reduction in seismic wave speeds at the crustal and uppermost mantle depth. A total of 35 200 models were generated during the first stage of the NA to ensure the convergence of the search. During the second stage, these models and their misfits were used to produce 1-D and 2-D marginals (Figs 7 and 8, respectively). The 1-D marginals are used to determine the posterior mean value and the corresponding standard error of each model parameter. A most likely (best-fitting) model can be obtained from the peak of the 1-D marginal distributions. The posterior mean model is shown as the solid line in Fig. 6(b) and the corresponding predicted dispersion curve is shown as the solid line in Fig. 6(a), which falls within data uncertainties.

The width of the 1-D marginal distributions shown in Fig. 7 demonstrates that *Vs* is better constrained in the three crustal layers than in the upper-mantle layers. The standard errors of *Vs* associated with the posterior mean model parameters are also shown as the grey area in Fig. 6(b). The shallow crust can be constrained better than the lower crust because short-period (dispersion) data has a narrower depth sensitivity kernel and, in particular, because the wave speed estimates for the lower crust structure trade-off strongly with the Moho depth. For this gridpoint the Moho depth is poorly constrained. The posterior mean Moho depth is 57.8 km with a standard error about 3 km. The posterior mean shear wave speeds (solid lines in Fig. 7) of the three crustal layers are very close to the most likely model, the peak of the corresponding 1-D marginals with approximate Gaussian distributions. For the five upper-mantle layers, the posterior mean shear wave speeds are also close to the most likely model, but generally with larger standard errors than those of the crustal layers, indicating that the long-period surface data which sample this depth range have relatively poorer depth resolution. The *Vs* of uppermost mantle layer (Moho—90 km) has the largest standard error (0.29 km s^{-1}), implying a large trade-off between Moho depth and the shear wave speed. The posterior mean shear wave speeds of both the middle crust and the lower crust are much lower than the *Vs* in the reference model (Figs 6b and 7). Relatively low shear wave speed also persists in one of the upper-mantle layer (90–130 km). However, from 130 to 280 km, the posterior mean *Vs* is higher than that of *ak135*.

The 2-D marginals (Fig. 8) illustrate the trade-off between different model parameters. The *Vs* in nearby layers shows apparent negative correlations. The trade-off between *Vs* of adjacent layers in the crust is smaller compared to trade-offs between *Vs* in nearby upper-mantle layers. This is a reflection of the fact that depth resolution is better for shorter than for longer period dispersion data. The Moho depth shows large trade-off (positive correlation) with the *Vs* in the lower crust and that in the uppermost mantle (Moho—90 km) (Fig. 8). Indeed, Moho depth cannot be constrained well with dispersion data alone because of the trade-off between the Moho depth and the wave speeds in the lower crust and uppermost mantle (Fig. 8). We recall, however, that we use the Moho depths from receiver function studies (Xu *et al.* 2007) as reference values in the NA search, which results in better estimations of the Moho depth than from dispersion data alone.

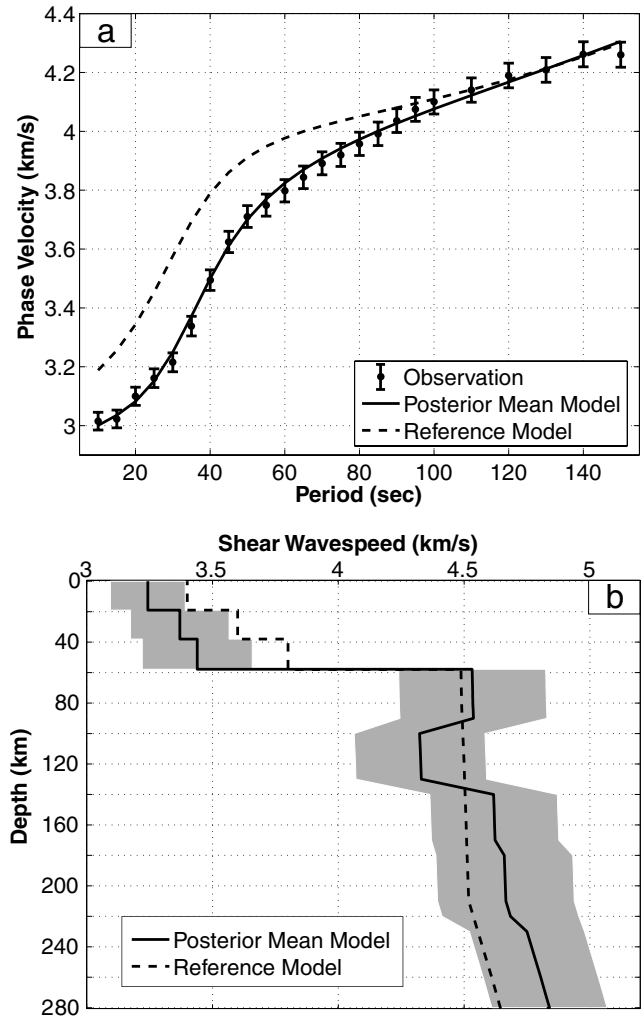

Figure 6. Rayleigh-wave phase velocity dispersion curves (a) and shear wave speed model (b) for the gridpoint at (101°E, 29°N) obtained from the NA. The observed dispersion data at the gridpoint are shown as the black dots in (a). The error bar on the observed dispersion point shows the standard error (1 per cent of the observed phase velocity) of the dispersion measurement at each period. The solid line in (b) shows the posterior mean *Vs* model and the predicted dispersion curve from this model is shown as the solid line in (a). The dashed line in (a) shows the predicted dispersion curve of the reference model [the dashed line in (b)], which consists of three crustal layers and mantle structure from the global *ak135* model (Table 1). The width of the shaded area shows the standard error of the posterior mean *Vs* in each layer.

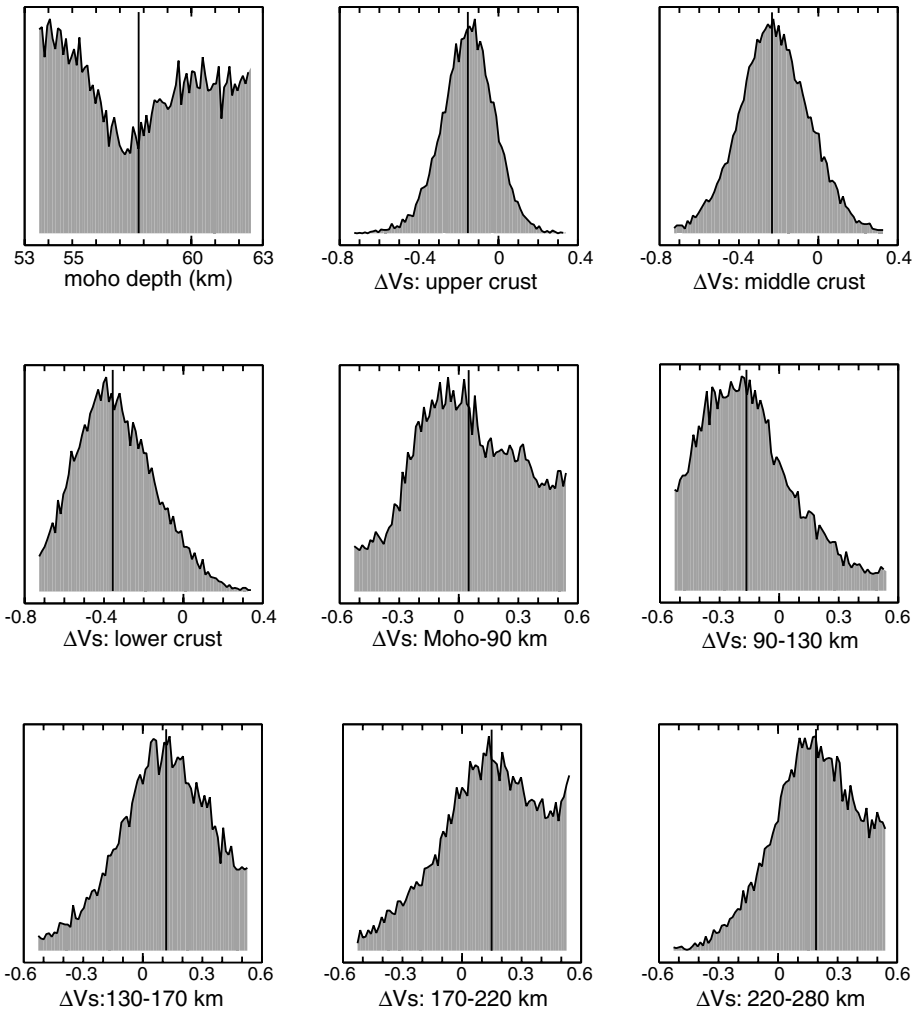

Figure 7. 1-D marginal posterior probability density functions (PPDFs) of the nine model parameters at (101°E, 29°N). The horizontal axis shows the variation range of Moho depth (km) or the perturbation range of ΔVs (km s^{-1}) for each layer as shown in Table 1 and the vertical axis is the normalized posterior probability density. In each plot, the solid line shows the parameter value of the posterior mean model. The reference Moho depth for this gridpoint is 58 km, and the posterior mean value from of the Moho depth from the 1-D marginal is 57.8 km with a standard error about 3 km. The almost flat 1-D marginal PPDF of the Moho depth implies the Moho depth is not well constrained at this gridpoint. Note that the posterior mean ΔVs of each crustal layer is very close to the value of the most likely model, which corresponds to the peak of each 1-D marginal PPDF with almost Gaussian distribution.

5 CRUSTAL AND UPPER-MANTLE STRUCTURE

From the 1-D posterior mean model and standard error inferred from the NA at each gridpoint, we infer 3-D wave speed variations, and their uncertainty, beneath the array. We will now present the inferred variation in Moho depth and images of *Vs* variations at different depths and along different vertical profiles.

5.1 Variation of Moho depth

In map view, the lateral variation in Moho depth beneath the array area is presented in Fig. 9. These results are, by design, consistent with the estimates by Xu *et al.* (2007). From west to east across the array the Moho depth decreases rather abruptly from 55–63 km in southwest Sichuan (i.e. the northwestern part of the array) to 37–45 km beneath the western margin of Sichuan basin. Southeastward the Moho depth (and crustal thickness) decreases more gradually to ∼40 km beneath central Yunnan. The 1-D marginals suggest that the standard error in Moho depth is 2–3 km.

5.2 3-D variation in shear wave speed

The lateral variation of *Vs* at 10, 25, 50, 75, 100 and 200 km depth is depicted in Fig. 10, with the uncertainties displayed in Fig. 11. Fig. 12 shows *Vs* heterogeneity along five vertical profiles from the surface to 250 km depth, with the uncertainties shown in Fig. 13.

In the Chuan-Dian Fragment (Fig. 1b, the magenta shaded area) the wave speed patterns vary significantly from the upper crust to the upper mantle. In the upper crust, high wave speed appears in the central and eastern part of this tectonic unit, while low wave speed mainly appears in the southern and western parts (Fig. 10a). The region northeast of the Red River fault (only the northern part is sampled in this study) shows prominent low wave speed in the upper crust (Fig. 10a), but this feature seems to disappear at larger depths. At the mid-crustal depth range, the northern Chuan-Dian Fragment is marked by a LVL, bounded to the south approximately by the Lijiang and Muli faults (Fig. 10b). Another prominent mid-crustal LVL appears in the southeastern part of Chuan-Dian Fragment, around the Luzhijiang-Xiaojiang fault zone (Fig. 10b; profiles CC′ and DD′ in Fig. 12). In the lower crust, a LVL appears in the

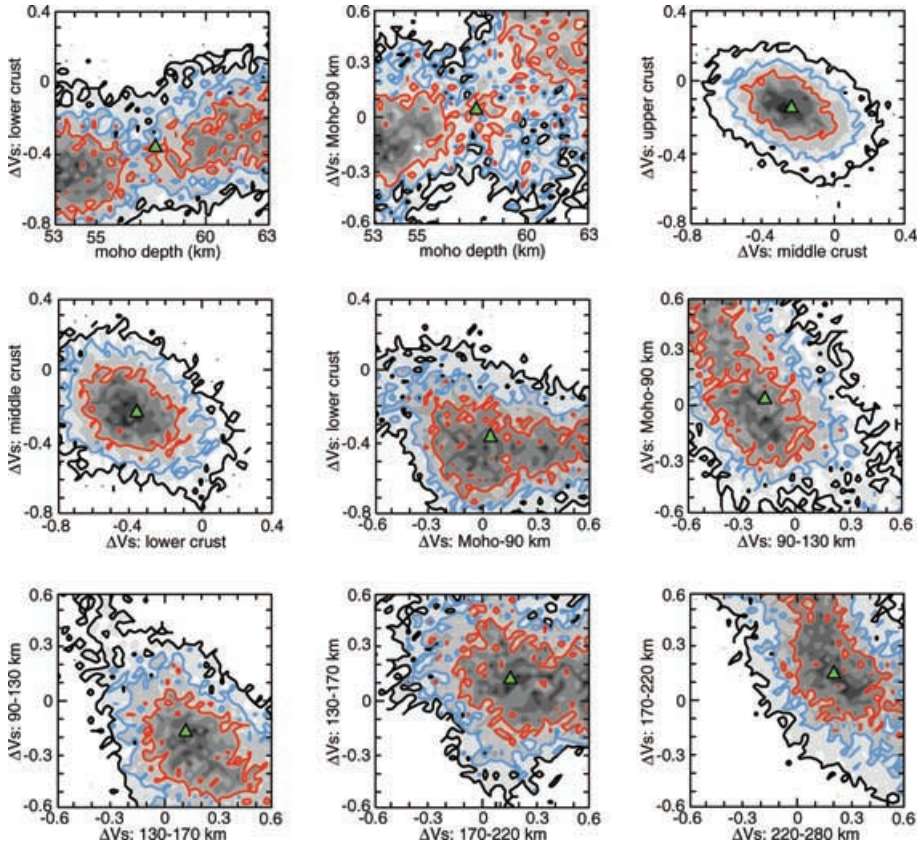

Figure 8. Examples of 2-D marginal PPDFs of the nine model parameters at (101°E, 29°N). In each panel, the values for the horizontal and vertical axis show the perturbation range of ΔVs (km s^{-1}) for each layer or the variation range of Moho depth (km). Black, blue and red lines are the contours to show 60, 90 and 99 per cent confidence level. The more circular and narrower the contour is, the smaller the trade-off between the two model parameters is. The posterior mean model is shown as a green triangle in each plot.

central part of Chuan-Dian Fragment, and in contrast to the middle crust the lower crust beneath northern portion is not anomalously slow (Fig. 10c; profiles AA′, BB′ and EE′ in Fig. 12). We note also that the LVL detected at mid-crustal depth beneath the northern Chuan-Dian Fragment (Fig. 10b) does not extend northeastward across the Xianshuihe fault (XSHF); in fact, normal shear wave speeds are observed northeast of this fault (profile AA′ in Fig. 12).

In the uppermost mantle (Fig. 10d), the eastern Chuan-Dian Fragment mainly appears slow while relatively high wave speeds prevail in part of the central fragment north of Lijiang fault. At 100 km depth (Fig. 10e), the northern Chuan-Dian Fragment is marked by low wave speeds while southern Chuan-Dian Fragment is relatively fast. The wave speed pattern at 200 km depth beneath the Chuan-Dian Fragment (Fig. 10f) seems to be quite different from that at 100 km depth, with low wave speed anomaly in the south fragment but high velocity anomaly in the northern fragment.

At very shallow depths, shear wave speed is slow in the western margin of Sichuan basin (Fig. 10a), probably due to presence of the thick sedimentary layers, but wave speed is high in the middle crust (Fig. 10b). The upper-mantle structure below the western margin of the Sichuan basin may be not reliable because the path coverage at intermediate and longer periods is poor (Fig. 4). Southwest of the Zhongdian–Dali–Red River fault the uppermost mantle (Moho—130 km) is relatively slow (Figs 10d and e), while at 200 km depth it changes to fast structure (Fig. 10f).

The average wave speeds in each layer of the study region are shown in Table 1. With respect to the reference value, we observe relatively low wave speeds in the three crustal layers and two uppermost mantle layers (Moho—90 km, 90–130 km) and higher wave speeds in other three deeper upper-mantle layers (130–170, 170–220 and 220–280 km). The average crustal velocity is about 3.47 km s^{-1}, which is about 4.3 per cent lower than that (∼3.63 km s^{-1}) of the global *ak135* (continental) crustal model.

6 DISCUSSION

The variation of the 3-D shear wave speed structure in the crust and upper mantle beneath the array area (up to about ±8 per cent variation with respect to the average value) is much larger than suggested by traditional (larger scale, but lower resolution) surface wave tomography. The inferred heterogeneity reflects a complicated (tectonic) transition from the Tibetan Plateau (Lhasa block, Qiangtang block and Songpan-Ganze Fold Belt) to the South China Block and Indo-China Block. Our results suggest that boundaries between major tectonic units identified at the surface appear to involve much—if not all—of the crust, and in some cases the uppermost mantle as well.

6.1 Uncertainties of the shear wave speeds from NA

Fig. 11 shows the standard errors (or uncertainties) of shear wave speeds for horizontal profiles at different depths in Fig. 10, and Fig. 13 shows the standard errors of shear wave speeds for vertical

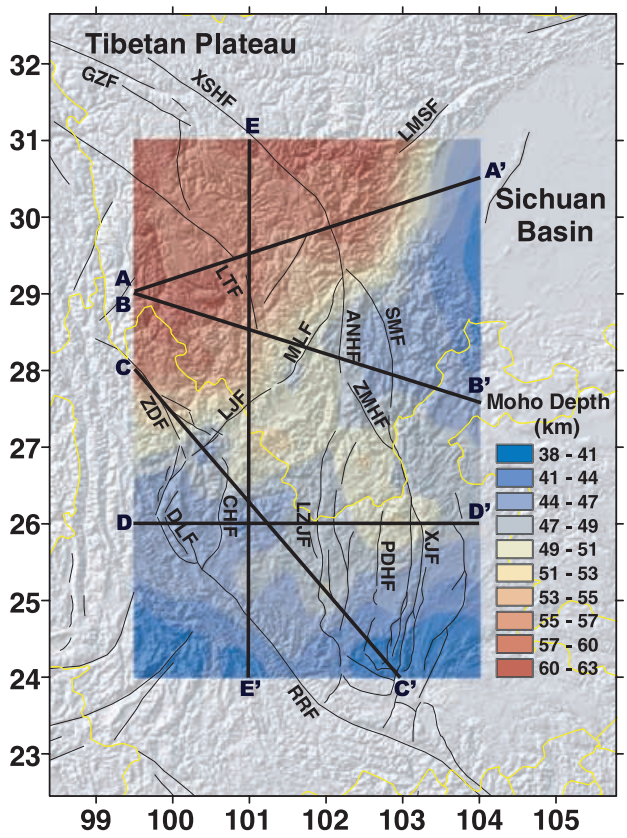

Figure 9. Variation of the Moho depth as inferred from the posterior mean model using the NA at each gridpoint in the studied area. The colour bar in the right corner shows the value of Moho depth. The black thick lines are the section lines of the vertical profiles (AA′, BB′, CC′, DD′ and EE′) shown in Fig. 12.

profiles in Fig. 12. The standard errors in the shear wave speed estimates are relatively small (∼0.15–0.2 km s^{-1}) at upper and middle crustal depth but larger (∼0.2–0.3 km s^{-1}) in the lower crust and the upper-mantle layers (Figs 11 and 13). This is due to the trade-offs with Moho depth and to the evanescent properties of surface waves at different periods: shorter period surface waves have a better depth sensitivity in the shallow crust, whereas longer period surface waves sample the upper-mantle structure with a much broader depth sensitivity kernel which results in a relatively poor depth resolution in the upper mantle.

At a given depth, the standard errors vary laterally (Figs 11 and 13) because of the lateral variability in model parametrization of the crust and upper-mantle layers (Section 4.2) and lateral variations in standard error of phase velocity. Estimating the uncertainties on the 2-D phase velocity maps directly from the uncertainties on the interstation measurements is still difficult at this stage. This is why we made a rough estimate using 1 per cent of the phase velocity determined at every period for each gridpoint.

The wave speed error is generally inversely proportional to layer thickness. For example, in the uppermost mantle layer (Moho—90 km) the largest uncertainties occur in regions where the Moho is deepest and, hence, the layer thinnest [i.e. in the northwestern part of the study region (Figs 9 and 11d)]. Setting the thickness of the upper and middle crust layer both about 1/3 of the total crustal thickness prevents any of these layers to become arbitrarily thin. The wave speed uncertainty is generally larger in the lower crust than in the upper and middle crust (Figs 11 and 13) because of the reduced sensitivity of the data and also because of the trade-off between Moho depth and the wave speed of the lower crust.

The uncertainty maps suggest that the LVLs in the middle crust, for example, in the northern Chuan-Dian Fragment and the Luzhijiang-Xiaojiang fault zone, are robust. Also the LVL in the lower crust beneath the central Chuan-Dian Fragment seems to be well resolved (Figs 13b, c and e). Some of the structures in the upper mantle have larger uncertainties. Because we performed a model space search that provided PPDFs for each model parameter, we have an overview of all the models compatible with the data. We did not choose a particular model based on regularization, as we would with a more traditional inverse method. In addition, because we carefully sampled the model space (with appropriate choice of the tuning parameters to make a broad sampling), we are confident that the models we obtained are not associated with local minima of the misfit function.

6.2 Heterogeneity of Chuan-Dian Fragment

The Chuan-Dian Fragment is usually regarded as a unique tectonic terrane and is thought to play an important role in the dynamics and tectonics of the eastern part of the Tibetan Plateau. According to recent GPS studies (King *et al.* 1997; Chen *et al.* 2000; Zhang *et al.* 2004; Shen *et al.* 2005) this block is moving southeastward at a rate larger than adjacent crust, which indicates that the crustal material is transported from the central part of the Tibetan Plateau to SW China and Burma around the EHS by clockwise rotation. However, the Chuan-Dian Fragment is not tectonically uniform, and on the basis of geological and geodetic studies one can identify different tectonic units (Wang *et al.* 1998; Wang & Burchfiel 2000; Shen *et al.* 2005).

Our results confirm that the crust and upper mantle beneath the Chuan-Dian Fragment are highly heterogeneous. At the surface, the Xianshuihe-Xiaojiang left-lateral fault system acts as the boundary between the Chuan-Dian Fragment and the South China block (which comprises the Yangtze Craton and the South China Fold Belt). In the northern part of the study region, we observe large wave speed contrasts across the Xianshuihe fault at the mid-crustal depth (Fig. 10b). Further south, and at larger depths, the Xiaojiang fault is not evident in the images. Further study must establish if this is a resolution issue or if it reflects spatial variations in character of and elastic properties across the fault. The data also reveal substantial contrasts across the Lijiang-Muli fault system (Fig. 10), which suggests that it is a main boundary within the Chuan-Dian Fragment. This inference is consistent with results from (surface) block modelling using GPS data (Shen *et al.* 2005), which identifies a northern block (including the Yajiang and Shangrilla subblocks) and a southern block (the Central Yunnan subblocks), separated by the Lijiang-Muli fault. The Lijiang-Muli fault is also part of the boundary between the Songpan-Ganza Fold Belt and the Yangtze Craton (Fig. 1b).

6.3 Crustal weak zones and the importance of faults

The tomographic images of the continental lithosphere demonstrate that LVLs are ubiquitous in the middle/lower crust and upper mantle beneath the southeastern borderland of the Tibetan Plateau. This is consistent with previous results (e.g. Huang *et al.* 2002; Wang *et al.* 2003; Hu *et al.* 2005a,b; Xu *et al.* 2007), but because of superior

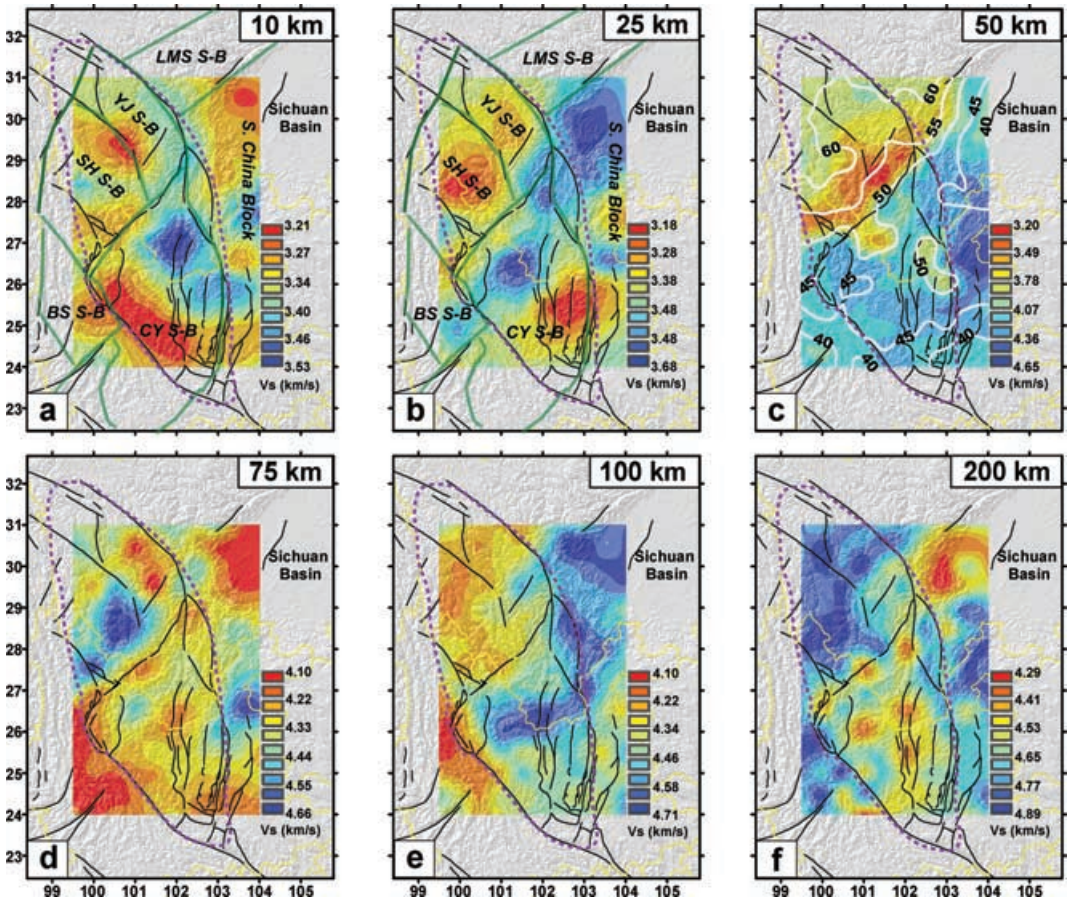

Figure 10. Variation in shear wave speed relative to the posterior mean model inferred from the NA: (a) 10 km; (b) 25 km; (c) 50 km; (d) 75 km; (e) 100 km and (f) 200 km. The major faults are depicted as thin black lines – for abbreviations see Fig. 1(b). The thick dark green lines are the block boundaries from the surface GPS data modelling (Shen *et al.* 2005). The abbreviations for subblocks are YJ (Yajiang), SH (Shangrilla), CY (Central Yunnan), LMS (Longmenshan) and BS (Baoshan) subblock (S-B). The white lines in (c) are the contour lines of Moho depth and the values are shown as the black numbers on them. The colour bar in the right corner of each plot shows the value of shear wave speed (km s^{-1}).

depth resolution we can determine, more confidently, the depth and lateral continuity of these LVLs.

High regional surface heat flow values (Hu *et al.* 2000) indicate steep geothermal gradients. The high geothermal gradient can reduce the shear wave speed and may cause partial melt in the crust. Partial melt of the crustal material in the Tibetan Plateau has been suggested by other studies, for example, partially molten in the middle crust beneath southern Tibet (Nelson *et al.* 1996; Unsworth *et al.* 2005), and in the mid-lower crust and upper mantle beneath northern Tibet (Meissner *et al.* 2004; Wei *et al.* 2001). It thus seems reasonable to attribute the large (>10 per cent), local reductions in shear wave speed to a reduction in rigidity due to elevated temperatures and, perhaps, partial melt in the middle or lower crust. Even small melt fractions would reduce the strength of the lithosphere (Kohlstedt & Zimmerman 1996) and facilitate intracrustal (plastic) flow due to external tectonic forces. From analysis of seismic anisotropy, Shapiro *et al.* (2004) and Ozacar & Zandt (2004) argued that channel flow is likely within the middle or middle-to-lower crust beneath the central parts of the plateau. The argument of crustal channel flow is further supported by the very low equivalent elastic thickness ($0 < T_e < 20$ km) beneath the Tibetan Plateau and SW China (Jordan & Watts 2005), and by the detection of zones of high (electric) conductivity in the crust of our study region (Sun *et al.* 2003; Bai *et al.* 2006).

The presence (or absence) of weak zones is important for our understanding of the geological development of the Tibetan Plateau. Indeed, geodynamic modelling involving gravity and/or thermal driven lateral flow within a weak middle/lower crust channel has been used to explain the tectonics in the Himalayan–Tibetan orogen (e.g. Beaumont *et al.* 2004) and eastern Tibet (e.g. Royden *et al.* 1997; Clark & Royden 2000; Shen *et al.* 2001). But many first-order issues about such weak layers have remained unresolved. The (geographical and depth) distribution of and interconnectivity between LVLs—and, by implication, the 3-D geometry of the presumed channel flow—are not well known. Can flow occur freely over large regions or are there local structures (such as faults) that interrupt or deflect flow? And what is effect of the asthenospheric upper mantle on crustal channel flow? Answering these questions will be of key importance for understanding the (tectonic) block motions inferred from GPS data and—indeed—regional seismicity.

In northern Tibet, the possible weak channel due to partial melt is likely to exist from the middle crust to upper mantle (Meissner *et al.* 2004; Wei *et al.* 2001). In southern Tibet, beneath the Himalayan orogen, many geophysical observations (e.g. Nelson *et al.* 1996; Unsworth *et al.* 2005) suggest that the partial melt and the consequent weaker channel probably dominate in the middle crust. In southeastern Tibet, lower crustal flow models (e.g. Royden *et al.* 1997) explain many geological aspects, such as

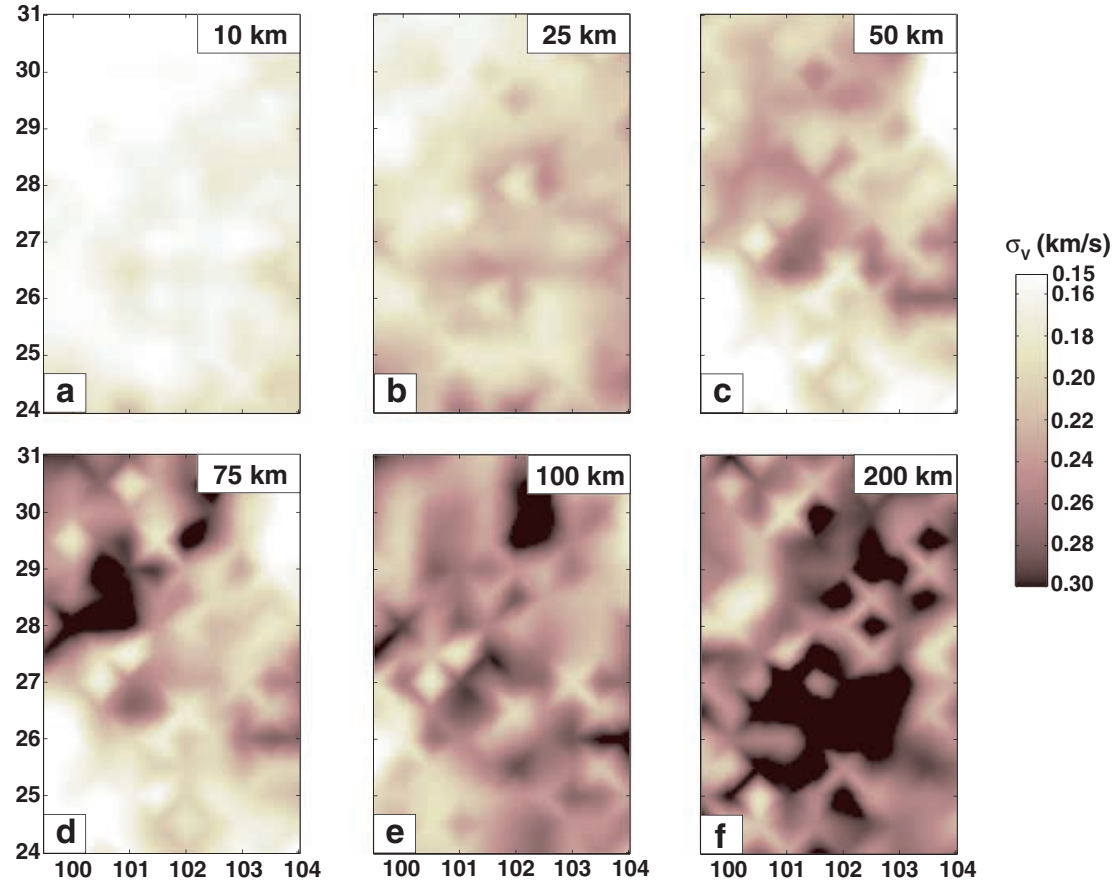

Figure 11. Standard error (σ_v) of the shear wave speed at different depths shown in Fig. 10. The colour bar in the right shows the value of σ_v (km s^{-1}).

the lack of young crustal shortening and the gentle topographic slope.

Our high-resolution surface wave array tomography reveals considerable regional variations in the strength and depth range of LVLs. In the northern part of the Chuan-Dian fragment and the Luzhijiang-Xiaojiang fault zone, the images reveal a mid-crustal LVL with a (horizontal) E-W extent of 150–200 km. In the central Chuan-Dian Fragment, the data require LVL in the lower crust. The high-resolution (3-D) images are beginning to suggest that some major fault zones in this area (e.g. Xianshuihe fault, Litang fault and Luzhijiang fault) mark lateral transitions in the mid- or lower crustal LVZs. This crustal heterogeneity implies that the flow pattern is more complicated and, in particular, that some of the major faults seem to play a more important role than assumed in the current generation of middle or lower crustal flow models. A better understanding of these structural relationships requires even higher resolution images of the crust beneath this region. This can be achieved through a combination of denser array deployments and the use of more powerful inverse scattering or (full wave) inversion approaches (e.g. De Hoop *et al.* 2006).

7 SUMMARY

We have used dispersion data from EGF and TS analysis to construct high-resolution Rayleigh wave phase velocity maps in the period band 10–150 s in the southeastern borderland of the Tibetan Plateau. These phase velocity maps were then inverted for 3-D shear wave speed variations in the study region using the NA. With NA, a global optimization method, we estimated parameter trade-offs and uncertainties. Because of the large trade-off between the Moho depth and the shear wave speed in the lower crust and uppermost mantle, we constrain the Moho depth using results from receiver function studies (Xu *et al.* 2007). The 15 per cent peak-to-peak variation of shear wave speed implies a complicated tectonic make up of the southeastern borderland of the Tibetan Plateau. The shear wave speed in the shallow crust beneath Chuan-Dian Fragment is characterized by regions with high and low velocity anomaly separated by some of the major faults, which is consistent with the tectonic and GPS studies and implies that Chuan-Dian Fragment is not a uniformly rigid block. Prominent LVLs have been found in the middle crust beneath the northern Chuan-Dian Fragment and the Luzhijiang-Xiaojiang fault zone and in the lower crust beneath the central Chuan-Dian Fragment.

The high-resolution images are beginning to reveal relationships between major faults in the area and the occurrence and lateral extent of crustal LVLs. The heterogeneous spatial distribution of the LVLs in the middle or lower crust in the southeastern borderland of the Tibetan Plateau and the possible interaction of the major faults with deep crustal structure suggest that the pattern of the possible crustal channel flow is complicated and may involve both middle and lower crustal flow. Establishing the relationship between major fault systems and the spatial distribution of crustal weak zones is of key importance for our understanding of the regional block motion (as inferred from GPS) and seismicity. These structural relationships are not yet fully resolved with the data coverage and inversion techniques used here, but we anticipate that new array deployments

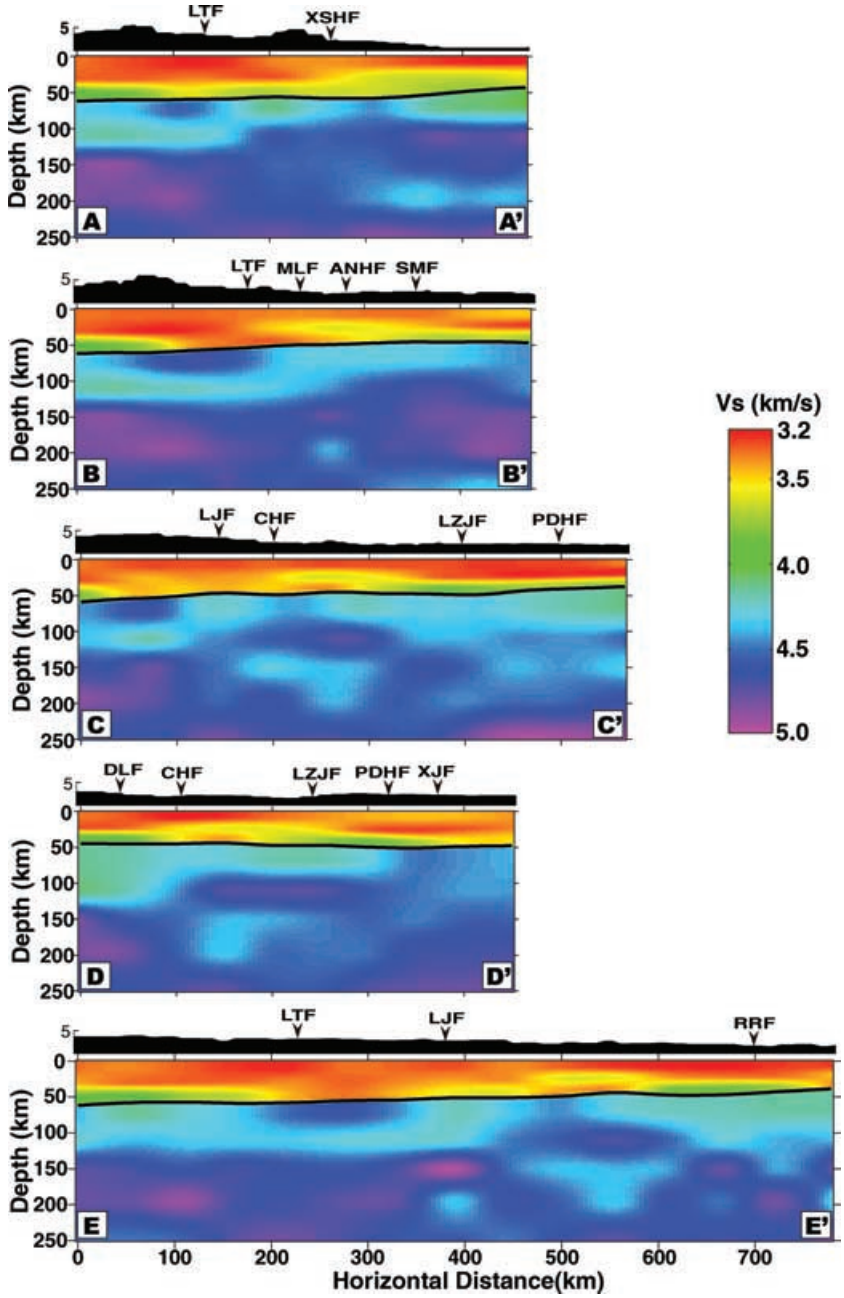

Figure 12. Shear wave speed variation relative to the posterior mean model inferred from the NA along five vertical profiles (AA′, BB′, CC′, DD′ and EE′ shown in the bottom of each plot; for location, see Fig. 9). The wave speed (km s^{-1}) colour scale is shown in the right. Topography is depicted above each profile (black area) and the arrows above it mark the location of major faults along each profile. The abbreviations for fault names are the same as in Fig. 1(b). The black line (around 50 km depth) on each colour profile indicates the Moho discontinuity.

and the use of more powerful combinations of interferometry and full wave inversion methods will change this situation in the not too distant future.

ACKNOWLEDGMENTS

We thank the Editor Jeannot Trampert and two anonymous reviewers for their constructive comments, which helped us improve the manuscript. We also thank Dr Malcolm Sambridge for providing us the source code of the NA, Prof Denghai Bai at the Institute of Geology and Geophysics Chinese Academy of Science and Jiangning Lü at MIT for sharing their results for comparison, Prof Qiyuan Liu at Chinese Earthquake Administration for helpful discussions and Dr Yaoqiang Wu and his research staff at Sichuan Earthquake Administration, China for their discussions and hospitality during our visit to Chengdu, China. This work was supported by the Continental Dynamics Program of the US National Science Foundation under grant 6892042.

REFERENCES

Bai, D., Meju, M., Arora, B., Ma, X., Jiang, C., Zhou, Z., Zhao, C., Wang, L., 2006. Large crustal-mantle channel flow in central Tibet and eastern Himalaya inferred from magnetotelluric models, *Eos Trans. AGU,* **87**(36), West. Pac. Geophys. Meet. Suppl., Abstract S45A-07.

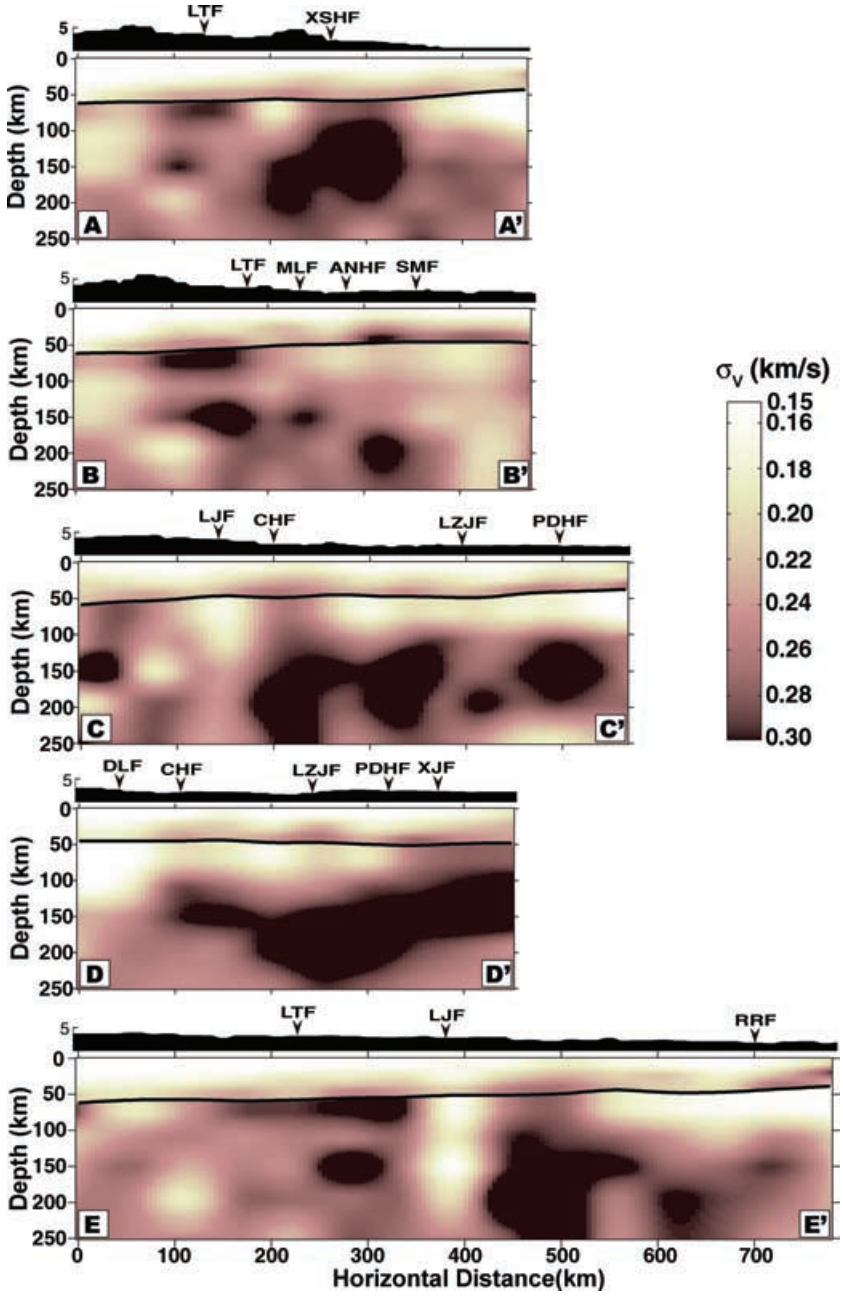

Figure 13. Standard error (σ_v) of the shear wave speed along five vertical profiles shown in Fig. 12. The colour bar in the right shows the value of σ_v (km s^{-1}).

Beaumont, C., Jamieson, R.A., Nguyen, M.H. & Medvedev, S., 2004. Crustal channel flow: 1. Numerical models with applications to the tectonics of the Himalayan-Tibetan orogen, *J. geophys. Res.,* **109,** B06406, doi:10.1029/2003JB002809.

Beghein, C., Resovsky, J.S. & Trampert, J., 2002. P and S tomography using normal-mode and surface wave data with a neighbourhood algorithm, *Geophys. J. Int.,* **149,** 646–658.

Brocher, T.M., 2005. Empirical relations between elastic wavespeeds and density in the Earth's crust, *Bull. seism. Soc. Am.,* **95**(6), 2081–2092.

Chen, Z. *et al.*, 2000. Global positioning system measurements from eastern Tibet and their implications for India/Eurasia intercontinental deformation, *J. geophys. Res,* **105,** 16 215–16 227.

Clark, M. & Royden, L.H., 2000. Topographic ooze: building the eastern margin of Tibet by lower crustal flow, *Geology,* **28**(8), 703–706.

De Hoop, M.V., van der Hilst, R.D., Shen, P., 2006. Wave-equation reflection tomography: annihilators and sensitivity kernels, *Geophys. J. Int.,* **167,** 1211–1214.

Hu, S., He, L. & Wang, J., 2000. Heat flow in the continental area of China: a new data set, *Earth planet. Sci. Lett.,* **179,** 407–419.

Hu, J.F., Su, Y.J., Zhu, X.G. & Chen, Y., 2005a. S-wave velocity and Poisson's ratio structure of crust in Yunnan and its application (in Chinese), *Sci. China Ser. D.,* **48**(2), 210–218.

Hu, J.F., Chu, X.G., Xia, J.Y. & Chen, Y., 2005b. Using surface wave and receiver function to jointly inverse the crust-mantle velocity structure in the West Yunnan area (in Chinese), *Chin. J. Geophys.,* **48**(5), 1069–1076.

Huang, J., Zhao, D. & Zheng, S., 2002. Lithospheric structure and its relationship to seismic and volcanic activity in southwest China, *J. geophys. Res.,* **107**(B10), 2255, doi:10.1029/2000JB000137.

Jordan, T.A. & Watts, A.B., 2005. Gravity anomalies, flexure and the elastic thickness structure of the India-Eurasia collisional system, *Earth planet. Sci. Lett.,* **236,** 732–750.

Kan, R., 1977. Study on the current tectonic stress field and the characteristics of current tectonics activity in southwest China (in Chinese), *Chin. J. Geophys.,* **20**(2), 96–107.

Kennett, B.L.N., Engdahl, E.R. & Buland, R., 1995. Constraints on the velocity structure in the earth from travel times, *Geophys. J. Int.,* **122,** 108–124.

King, R.W. *et al.*, 1997. Geodetic measurement of crustal motion in southwest China, *Geology,* **25,** 179–182.

Kohlstedt, D.L. & Zimmerman, M.E., 1996. Rheology of partially molten mantle rocks, *Annu. Rev. Earth planet. Sci.,* **24,** 41–62.

Lev, E., Long, M.D., Van der Hilst, R.D., 2006. Seismic anisotropy in eastern Tibet from shear wave splitting reveals changes in lithospheric deformation, *Earth planet. Sci. Lett.,* **251,** 293–304.

Li, Z.X., 1998. Tectonic history of the major East Asian lithosphere blocks since the mid-Proterozoic. in *Mantle Dynamics and Plate Interactions in East Asia,* pp. 211–243, ed. Flower, M. F. J., Chung, S.-L., Lo, C.-H., Lee, T.-Y. *Geodyn. Ser.*, 27.

Li, C., Van der Hilst, R.D. & Toksoz, M.N., 2006. Constraining P-wave velocity variations in upper mantle beneath Southeast Asia, *Phys. Earth planet. Inter.,* **154,** 180–195.

Li, C., Van der Hilst, R.D., Meltzer, A.S., Sun, R. & Engdahl, E.R., 2008. Subduction of the Indian lithosphere beneath the Tibetan Plateau and Burma, *Earth Planet. Sci. Lett.*, submitted.

Lin, F.-C., Ritzwoller, M.H., Townend, J., Bannister, S. & Savage, M.K., 2007. Ambient noise Rayleigh wave tomography of New Zealand, *Geophys. J. Int.,* **170**(2), 649–666. doi:10.1111/j.1365–246X.2007.03414.x

Masters, G., Laske, G., Bolton, H. & Dziewonski, A., 2000. The relative behavior of shear velocity, bulk sound speed, and compressional velocity in the mantle: implications for chemical and thermal structure, *Geophys. Monogr. Ser.,* **117,** 63–87.

Meissner, R., Tilmann, F. & Haines, S., 2004. About the lithospheric structure of central Tibet, based on seismic data from the INDEPTH III profile, *Tectonophysics,* **380,** 1–25.

Molnar, P. & Tapponnier, P., 1975. Cenozoic tectonics of Asia: effects of a continental collision, *Science,* **189,** 419–426.

Mooney, W.D., Laske, G. & Masters, G., 1998. CRUST5.1: a global crustal model at $5^\circ \times 5^\circ$, *J. geophys. Res.,* **103,** 727–747.

Nelson, K.D., Zhao, W. J., Brown, L. D., Kuo, J., Che, J., Liu, X., Klemperer, S. L. & Makovsky, Y., 1996. Partially molten middle crust beneath Southern Tibet: synthesis of Project INDEPTH results, *Science,* **294,** 1684–1688.

Nolet, G., 1985. Solving or resolving inadequate and noisy tomographic systems, *J. Comput. Phys.,* **61,** 463–482.

Ozacar, A. & Zandt, G., 2004. Crustal seismic anisotropy in central Tibet: implications for deformational style and flow in the crust, *Geophys. Res. Lett.,* **31,** L23601, doi:10.1029/2004GL021096.

Resovsky, J.S. & Trampert, J., 2002. Reliable mantle density error bars: an application of the neighbourhood algorithm to normal-mode and surface wave data, *Geophys. J. Int.,* **150,** 665–672.

Rowley, D.B., 1996. Age of initiation of collision between India and Asia: a review of stratigraphic data, *Earth planet. Sci. Lett.,* **145,** 1–13.

Royden, L.H., Burchfiel, B. C., King, R. W., Wang, E., Chen, Z., Shen, F. & Liu, Y., 1997. Surface deformation and lower crustal flow in eastern Tibet, *Science,* **276,** 788–790.

Sabra, K.G., Gerstoft, P., Roux, P. & Kuperman, W.A., 2005. Surface wave tomography from microseisms in Southern California, *Geophys. Res. Lett.,* **32,** L14311, doi:10.1029/2005GL023155.

Sambridge, M., 1999a. Geophysical inversion with a neighbourhood algorithm – I. Searching a parameter space, *Geophys. J. Int.,* **138,** 479–494.

Sambridge, M., 1999b. Geophysical inversion with a neighbourhood algorithm – II. Appraising the ensemble, *Geophys. J. Int.,* **138,** 727–746.

Shapiro, N.M., Campillo, M., Stehly, L. & Ritzwoller, M.H., 2005. High-resolution surface wave tomography from ambient seismic noise, *Science,* **307,** 1615–1618.

Shen, F., Royden, L.H. & Burchfiel, B.C., 2001. Large-scale crustal deformation of the Tibetan Plateau, *J. geophys. Res.,* **106**(B4), 6793–6816.

Shen, Z.-K., Lü, J., Wang, M. & Bürgmann, R., 2005. Contemporary crustal deformation around the southeast borderland of the Tibetan Plateau, *J. geophys. Res.,* **110,** B11409, doi:10.1029/2004JB003421.

Simons, F.J. & Van der Hilst, R.D., 2003. Structure and deformation of the Australian lithosphere, *Earth planet. Sci. Lett.,* **211,** 271–286.

Snoke, J.A. & Sambridge, M., 2002. Constraints on the S-wave velocity structure in a continental shield from surface-wave data: comparing linearized least-squares inversion and the direct-search neighbourhood algorithm, *J. geophys. Res.,* **107**(B5), 2094, doi:10.1029/2001JB000498.

Sol, S. *et al.*, 2007. Geodynamics of southeastern Tibet from seismic anisotropy and geodesy, *Geology,* **35,** 563–566, doi:10.1130/G23408A.1.

Sun, J., Jin, G.W., Bai, D.H. & Wang, L.F., 2003. Electrical structure of the crust and upper mantle and tectonics sense on the edge of the East Tibet, *Science in China* (Series D) (in Chinese), **33** (Suppl.) 173–180.

Tapponnier, P., Xu, Z., Roger, F., Meyer, B., Arnaud, N., Wittlinger, G. & Yang, J., 2001. Oblique stepwise rise and growth of the Tibet Plateau, *Science,* **294,** 1671–1677.

Unsworth, M.J., Jones, A.G., Wei, W., Marquis, G., Gokarn, S.G. & Spratt, J.E., 2005. Crustal rheology of the Himalaya and southern Tibet from magnetotelluric data, *Nature,* **438,** 78–81.

Wang, E. & Burchfiel, B.C., 2000. Late Cenozoic to Holocene deformation in southwestern Sichuan and adjacent Yunnan, China, and its role in formation of the southeastern part of the Tibetan Plateau, *Geol. Soc. Am. Bull.,* **112,** 413–423.

Wang, E., Burchfiel, B.C., Royden, L.H., Chen, L., Chen, J., Li, W. & Chen, Z., 1998. Late Cenozoic Xianshuihe-Xiaojiang, Red River and Dali fault systems of southwestern Sichuan and central Yunnan, China, *Spec. Pap. Geol. Soc. Am.,* **327,** 1–108.

Wang, C.-Y., Chan, W.W. & Mooney, W.D., 2003. Three-dimensional velocity structure of crust and upper mantle in southwestern China and its tectonic implications, *J. geophys. Res.,* **108**(B9), 2442, 176–193, doi:10.1029/2002JB001973.

Wei, W. *et al.*, 2001. Detection of widespread fluids in the Tibetan crust by magnetotelluric studies, *Science,* **292,** 716–718.

Xu, L., Rondenay, S., Van der Hilst, R.D., 2007. Structure of the crust beneath the Southeastern Tibetan Plateau from teleseismic receiver functions, *Phys. Earth Planet. Int.,* doi:10.1016/j.pepi.2007.09.002.

Yang, Y., Ritzwoller, M.H., Levshin, A.L. & Shapiro, N.M., 2007. Ambient noise Rayleigh wave tomography across Europe, *Geophys. J. Int.,* **168,** 259–274.

Yao, H., Van der Hilst, R.D. & de Hoop, M.V., 2006. Surface-wave array tomography in SE Tibet from ambient seismic noise and two-station analysis—I. Phase velocity maps, *Geophys. J. Int.,* **166,** 732–744.

Yoshizawa, K. & Kennett, B.L.N., 2002. Non-linear waveform inversion for surface waves with a neighbourhood algorithm—application to multimode dispersion measurements, *Geophys. J. Int.,* **149,** 118–133.

Zhang, P. *et al.*, 2004. Continuous deformation of the Tibetan Plateau from global positioning system data, *Geology,* **32**(9), 809–812.

Zhang, Z., Bai, Z., Wang, C., Teng, J., Lu, Q., Li, J., Sun, S & Wang, Z., 2005. Crustal structure of Gondwana- and Yangtze-typed blocks: an example by wide-angle seismic profile from Menglian to Malong in western Yunnan, *Science in China* (Series D) (in Chinese), **48**(11), 1826–1836.